

# Class-Specific Branch Attention for Mitigating Gradient Interference under Class Imbalance

Arush Singhal<sup>a</sup>, Dr. Umang Soni<sup>b</sup>

<sup>a</sup>Thapar Institute of Engineering and Technology, Patiala, India

<sup>b</sup>Netaji Subhash University of Technology, New Delhi, India

---

## Abstract

Deep neural networks trained under severe class imbalance often exhibit degraded performance, typically attributed to statistical bias. In this work, we identify a complementary optimization-level pathology: inter-class gradient interference within shared representations, where gradients from majority classes suppress minority-class learning. To analyze this phenomenon, we introduce a diagnostic framework based on layer-wise gradient flow analysis and a Gradient Conflict Matrix, which quantifies interference using cosine similarity between class-specific gradients. Using this framework, we study multi-branch convolutional architectures and propose a lightweight modification, Class-Specific Branch Attention (CSBA), that enables branch-specific channel reweighting to reduce gradient coupling. This mechanism promotes implicit feature decoupling across branches while preserving architectural simplicity. Empirically, CSBA improves minority-class performance, increasing the F1 score for the Physical-Damage class from 0.261 to 0.522 under severe imbalance, while maintaining comparable overall accuracy. These results indicate that mitigating gradient interference can directly enhance minority-class representation. Validation on CIFAR-10-LT confirms that this behavior generalizes across imbalanced visual recognition settings, with Macro-F1 improving from 0.595 to 0.655. More broadly, our findings highlight the importance of considering optimization dynamics alongside statistical methods when designing architectures for imbalanced learning.

*Keywords:* Class imbalance, Gradient interference, Multi-branch neural networks, Attention mechanisms, Deep learning optimization, Imbalanced visual recognition

---

## 1. Introduction

Class imbalance is a pervasive challenge in visual recognition, arising whenever training data contains substantially more examples of some categories than others [1, 2]. In real-world classification systems—spanning industrial inspection, medical imaging, and long-tailed recognition—minority classes are often the most critical to identify correctly, yet standard training procedures systematically fail them [3, 4, 5]. The dominant approach has been to address imbalance at the data or loss level, through oversampling, cost-sensitive learning, or modified loss functions. However, these methods treat imbalance as a statistical phenomenon and do not account for how gradient signals propagate and interact within the network during training.

Convolutional Neural Networks (CNNs) have shown strong performance in visual recognition by learning hierarchical feature representations [6, 7]. Among CNN-based models, multi-branch architectures have emerged as a promising paradigm for improving feature diversity and robustness [8, 9]. By processing inputs through parallel pathways, these architectures learn complementary representations that capture different aspects of complex visual patterns. However, despite their representational strength, multi-branch CNNs degrade substantially under severe class imbalance. The summation-based fusion common to these architectures creates a structural pathology: gradient signals from majority classes accumulate across branches and dominate the shared representation, suppressing minority-class learning in a way that data-level and loss-level interventions do not directly

address.

In this work, we study this optimization-level failure mode systematically. We evaluate our approach on photovoltaic (PV) fault detection [10, 11], a domain characterized by severe real-world class imbalance, and additionally validate on CIFAR-10-LT [4] to confirm that the proposed framework generalizes broadly to any multi-branch architecture trained under imbalanced conditions.

*Contributions:*

- We identify inter-class gradient interference as a key optimization bottleneck in multi-branch architectures under class imbalance.
- We propose a diagnostic framework based on gradient cosine similarity to quantify this interference.
- We introduce Class-Specific Branch Attention (CSBA) to reduce gradient conflict through branch-specific feature modulation.
- We empirically show that CSBA improves gradient geometry while maintaining a favorable balance between branch specialization and parameter efficiency.
- We provide empirical evidence that performance under data scarcity benefits from jointly considering optimization dynamics and model capacity.

In the following sections, we first present the proposed diagnostic framework for analyzing gradient interference, followed by the CSBA architecture.

## 2. Related Work

### 2.1. Imbalanced Visual Recognition

Class imbalance has been extensively studied in the context of visual recognition [1, 2]. Long-tailed distributions are common in real-world datasets spanning medical imaging [12], industrial inspection [10], and scene understanding [13]. Models trained under such conditions tend to prioritize majority classes and fail to generalize to minority categories, even when those categories are operationally critical.

Data-level approaches such as oversampling and SMOTE attempt to rebalance the training distribution, while algorithm-level methods assign higher misclassification penalties to minority classes. Loss-level modifications, including Focal Loss [3], class-balanced loss [5], LDAM [4], and centroid-based approaches for improving tail-class representation [14], have shown strong results by adjusting gradient magnitudes according to class frequency or sample difficulty. Despite these advances, a common limitation remains: these methods treat imbalance as a statistical problem and do not consider how gradient signals from different classes interact within shared network representations during backpropagation.

### 2.2. Multi-Branch Architectures for Visual Recognition

A wide range of deep learning architectures has been explored for visual recognition under complex and imbalanced conditions, including classical CNNs, transfer-learning models, and segmentation-based frameworks. Pre-trained architectures such as VGG, ResNet, and Inception are commonly used because of their strong feature-extraction capabilities [8, 9]. These models leverage transfer learning to adapt knowledge from large-scale datasets, such as ImageNet, to PV-specific tasks, thereby improving performance under limited-data conditions.

Segmentation-based approaches, particularly those based on U-Net and its variants, have been used to localize defects before classification, enabling more precise fault identification [15]. These methods are especially useful for detecting fine-grained defects such as cracks or localized damage, which may not be captured effectively by global classification models.

In addition to standard architectures, recent work has focused on improving performance through architectural modifications. Techniques such as residual connections, feature fusion, and attention mechanisms have been introduced to strengthen representation learning. Squeeze-and-Excitation (SE) blocks, for example, are widely used to recalibrate channel-wise feature responses and allow models to emphasize more informative features [16, 17, 18, 12]. Similarly, multi-scale feature aggregation and hybrid architectures that combine convolutional and transformer-based modules have been explored to capture complex visual patterns.

Multi-branch architectures constitute another important class of models, in which multiple parallel pathways process input features. These architectures aim to improve robustness by learning

complementary representations across branches. By aggregating features from different pathways, the model can capture diverse aspects of the input, which is particularly beneficial in complex visual tasks. However, most existing work assumes balanced training conditions and does not explicitly analyze how multi-branch structures behave under class imbalance.

### 2.3. Class Imbalance in Visual Recognition

Class imbalance is a fundamental challenge in visual recognition because real-world datasets typically contain substantially more examples of common categories than rare but critical ones. This imbalance leads to biased learning, in which models prioritize majority classes and fail to recognize minority classes accurately [10, 2, 13].

To address this issue, a wide range of techniques has been proposed. Data-level methods include oversampling minority classes, undersampling majority classes, and generating synthetic samples with techniques such as SMOTE. Algorithm-level methods include cost-sensitive learning, in which higher penalties are assigned to the misclassification of minority classes. Loss-level modifications, such as Focal Loss, dynamically adjust the contribution of each sample according to its difficulty, improving performance on hard examples [3, 5, 4, 19, 20, 21].

Although these approaches have improved classification performance, they primarily treat imbalance as a statistical problem. As a result, they focus on adjusting data distributions or loss functions without considering how imbalance affects the internal optimization dynamics of deep networks. In particular, they do not address how gradient signals from different classes interact within shared feature representations, even though these interactions can strongly influence learning behavior.

### 2.4. Optimization Dynamics and Gradient Interference

Recent research has begun to examine the role of optimization dynamics in deep learning, particularly in settings involving multiple tasks or imbalanced data. In multi-task learning, it has been observed that gradients associated with different tasks may conflict, leading to suboptimal parameter updates and slower convergence. Various methods have been proposed to mitigate such conflicts, including gradient normalization, projection, and balancing techniques [22, 23].

However, these approaches are designed primarily for multi-task learning and are not directly tailored to single-task classification under class imbalance. In multi-branch architectures, a related phenomenon arises when gradients from different classes interact within shared layers. Under imbalanced conditions, gradients from majority classes dominate the optimization process, potentially suppressing or distorting contributions from minority classes.

Despite its importance, this phenomenon—which we refer to as inter-class gradient interference—has received limited attention in the context of visual classification under class imbalance. Existing studies focus primarily on improving accuracy through architectural complexity or loss design without explicitly analyzing gradient interactions. As a result, the underlying causes of performance degradation in imbalanced multi-branch networks remain poorly understood.

## 2.5. Summary and Research Gap

In summary, prior work on imbalanced visual recognition has made substantial progress using both classical machine learning and deep learning techniques. However, several limitations remain. First, most approaches address class imbalance at the data or loss level without considering its effect on optimization dynamics. Second, although advanced architectures such as multi-branch networks and attention-based models have improved feature representation, their behavior under imbalanced conditions remains poorly understood. Third, existing methods rarely provide a detailed analysis of how gradient interactions influence feature learning in deep networks.

Existing approaches such as focal loss, LDAM, and Balanced Softmax primarily address class imbalance at the loss level [3, 4, 5, 20]. In contrast, our method targets the optimization dynamics within the network architecture, making it complementary to these approaches rather than directly competing with them.

To the best of our knowledge, there is limited work that systematically investigates inter-class gradient interference in multi-branch architectures or proposes structural mechanisms to mitigate it. This gap motivates our work, in which we explicitly analyze gradient interactions using a diagnostic framework and introduce an attention-based architectural modification to enable feature decoupling. By shifting the focus from statistical imbalance to optimization behavior, our approach offers a new perspective on learning under imbalanced conditions and provides practical design insights for real-world applications.

## 3. Methodology

We address multi-class fault classification in photovoltaic (PV) systems under severe class imbalance. Our methodology proceeds in four stages: (i) formal problem setup, (ii) a multi-branch baseline architecture, (iii) gradient conflict analysis to diagnose optimization pathologies, and (iv) Class-Specific Branch Attention (CSBA) to mitigate identified failure modes. Throughout, we maintain a dual focus on optimization geometry and parameter efficiency, arguing that reducing gradient conflict must be balanced carefully against network capacity to maintain robustness in data-scarce settings.

### 3.1. Problem Formulation

Let  $\mathcal{D} = \{(x_i, y_i)\}_{i=1}^N$  denote a labeled dataset where  $x_i \in \mathbb{R}^{B \times 3 \times 227 \times 227}$  is an RGB image of a PV panel and  $y_i \in \{1, \dots, C\}$  is its fault class label, with  $C = 6$  classes. The empirical class distribution  $p(y)$  is highly skewed, introducing systematic bias into gradient-based optimization.

The objective is to learn a classifier  $f_\theta$  where predictions are obtained via:

$$\hat{y} = \text{Softmax}(f_\theta(x)) \quad (1)$$

To counteract class imbalance at a fundamental level, training minimizes an explicitly class-weighted cross-entropy objective:

$$\mathcal{L}_{\text{CE}} = - \sum_{c=1}^C w_c y_c \log \hat{y}_c \quad (2)$$

where  $w_c$  is an inverse-frequency class weight computed directly from the training distribution (yielding [0.759, 0.748, 0.687, 1.542, 2.290, 1.239]):

$$w_c = \frac{N}{C \cdot N_c} \quad (3)$$

The Physical-Damage class receives the largest class weight ( $w_c = 2.29$ ), constituting the primary statistical mitigation of class imbalance during training.

### 3.2. Baseline Multi-Branch Architecture

Our baseline model adopts a modified SqueezeNet-inspired architecture comprising a shared backbone followed by parallel classification branches.

#### 3.2.1. Feature Extraction Backbone

Given input  $x$ , an initial stem block produces a low-level feature map:

$$F_{\text{stem}} = \text{MaxPool}(\delta_{0.01}(\text{BN}(\text{Conv}_{3 \times 3}(x)))) \quad (4)$$

where  $\delta_{0.01}$  denotes the LeakyReLU activation (formally defined in Eq. 18), with negative slope  $\alpha = 0.01$ . LeakyReLU prevents dead neuron pathologies that are particularly harmful for minority-class representations receiving extremely sparse gradient updates.

The network then applies a sequence of exactly eight modified Fire modules ( $M_2$  through  $M_9$ ). Formally, each transforms its input  $F_{\text{in}}$  as follows:

$$S = \delta_{0.01}(\text{BN}(\text{Conv}_{1 \times 1}(F_{\text{in}}))) \quad (5)$$

$$E_1 = \delta_{0.01}(\text{BN}(\text{Conv}_{1 \times 1}(S))) \quad (6)$$

$$E_2 = \delta_{0.01}(\text{BN}(\text{Conv}_{3 \times 3}(S))) \quad (7)$$

$$E_3 = \delta_{0.01}(\text{BN}(\text{Conv}_{3 \times 3}(S))) \quad (8)$$

Their outputs are linearly concatenated ( $F_{\text{out}} = \text{Concat}(E_1, E_2, E_3)$ ). After all eight modules, interspersed with max-pooling operations, the final shared representation is:

$$F_9 \in \mathbb{R}^{B \times 768 \times 14 \times 14} \quad (9)$$

#### 3.2.2. Multi-Branch Classification Head

The tensor  $F_9$  is routed into  $K = 3$  parallel branches via dropout ( $p = 0.5$ ):

$$o_k = \text{Conv}_{1 \times 1}(\text{Dropout}_{0.5}(F_9)), \quad k \in \{1, 2, 3\} \quad (10)$$

Branch outputs are aggregated via element-wise summation ( $O = \sum_{k=1}^3 o_k$ ), and  $O$  serves as the final logit tensor. As we show next, this symmetric structure implies that majority-class gradients can dominate and suppress minority representations.

### 3.3. Gradient Coupling Analysis

During backpropagation, gradients accumulate at the shared representation  $F_9$ :

$$\frac{\partial \mathcal{L}}{\partial F_9} = \sum_{k=1}^3 \frac{\partial \mathcal{L}}{\partial o_k} \cdot \frac{\partial o_k}{\partial F_9} \quad (11)$$

Although class-weighted loss partially scales signal magnitude, summation-based fusion functionally combines gradient directions for majority classes while attenuating minority-class signals. To quantify this interference rigorously, we compute pairwise gradient cosine similarities over flattened model parameters:

$$S_{ij} = \frac{\mathbf{g}_i^\top \mathbf{g}_j}{\|\mathbf{g}_i\|_2 \|\mathbf{g}_j\|_2 + \epsilon} \quad (12)$$

We organize these into a Gradient Conflict Matrix  $\mathbf{G}$ , summarizing global interference geometry at convergence.

For the baseline architecture, the global average over all  $C(C-1) = 30$  class pairs yields  $\bar{S}_{\text{global}} = -0.077 \pm 0.331$ , indicating the presence of destructive gradient interactions between class representations. When averaged over the six majority–minority pairs with the strongest interference (reported in Table 4), this statistic is  $\bar{S}_{\text{pairs}} = -0.236$ ; we use this subset-specific value in the optimization–generalization analysis of Section 4.5 to highlight the worst-case interference regime.

### 3.4. Class-Specific Branch Attention (CSBA)

To mitigate gradient interference, we introduce Class-Specific Branch Attention (CSBA), applied directly before multi-branch routing.

For each branch  $k \in \{1, 2, 3\}$ , CSBA first computes a compact global descriptor from  $F_9$  via global average pooling:

$$\mathbf{z} = \text{GAP}(F_9) \in \mathbb{R}^{768} \quad (13)$$

The attention vector  $\mathbf{a}_k$  is produced by a branch-specific two-layer bottleneck:

$$\mathbf{a}_k = \sigma(\Theta_{k,2} \cdot \delta(\Theta_{k,1} \mathbf{z})) \quad (14)$$

where  $\Theta_{k,1} \in \mathbb{R}^{96 \times 768}$  and  $\Theta_{k,2} \in \mathbb{R}^{768 \times 96}$  are branch-specific bias-free projection matrices,  $\delta$  denotes ReLU, and  $\sigma$  denotes sigmoid.

**Zero-Bias Constraint:** The projection matrices  $\Theta_{k,1}$  and  $\Theta_{k,2}$  are bias-free. Omitting bias terms encourages each module to respond to relative differences in channel activation magnitudes rather than learning class-independent offsets, which would otherwise reduce the channel selectivity that drives branch specialization.

Applying Hadamard multiplication:

$$\mathbf{F}'_k = F_9 \odot \text{Reshape}(\mathbf{a}_k, [B, 768, 1, 1]) \quad (15)$$

This channel-wise reweighting induces branch-specific Jacobians  $\text{diag}(\mathbf{a}_k)$  during backpropagation, formally analyzed in Section 4.

Hyperparameter	Value
Optimizer	Adam
$\beta_1, \beta_2$	0.9, 0.999
Initial LR $\eta_0$	$1 \times 10^{-4}$
LR Schedule	StepLR ( $\gamma = 0.95$ , $s = 23$ epochs)
Early Stopping	Patience = 30 epochs
Dropout rate	$p = 0.5$ per branch
Loss function	Class-weighted cross-entropy ( $w_c$ )
Batch size	64
Max epochs	300 (subject to early stopping)

Table 1: Fixed training protocol used across all model variants to ensure consistent optimization conditions.

#### 3.4.1. Parameter Overhead

Each branch introduces exactly two bias-free projection matrices:  $(96 \times 768) + (768 \times 96) = 147,456$  weights per branch, for a total overhead of  $3 \times 147,456 = 442,368$  parameters. The resulting model sizes are:

$$|\theta_{\text{baseline}}| = 1.35\text{M}, \quad |\theta_{\text{CSBA}}| = 1.79\text{M} \quad (16)$$

This represents a 32.6% increase relative to the baseline parameter count.

### 3.5. Optimization and Training Protocol

All model variants are trained under the same protocol, with weights initialized using Kaiming uniform initialization.

#### 3.6. Optimization-Generalization Equilibrium

Architectures employing fully segregated pathways (e.g., Class-Specific Heads) achieve strong gradient isolation but at substantial parameter cost. Such approaches increase parameter counts from 1.35M to prohibitive levels ( $\approx 7.50\text{M}$ ), making deployment on resource-constrained devices impractical in industrial environments.

Our analysis shows that CSBA provides a favorable balance. Under CSBA, the global average conflict shifts to  $\bar{S}_{\text{global}} = -0.096 \pm 0.313$ . The reduction in standard deviation from  $\pm 0.331$  to  $\pm 0.313$  indicates a contraction of extreme pairwise conflicts across the class distribution, while the 32.6% parameter overhead remains modest relative to the minority-class gains reported in Section 7.

## 4. Proposed Architectures and Optimization Formulations

To systematically study and mitigate inter-class gradient interference in shared-representation networks under severe class imbalance, we develop a comprehensive architectural framework grounded in both theoretical analysis and empirical validation. The framework proceeds in four stages. First, we formalize the shared backbone as a modified tri-path feature extractor and characterize the representational geometry of its output tensor. Second, we define the baseline multi-branch topology and show that its summation-based fusion structurally induces gradient coupling under class imbalance. Third, we introduce Class-Specific

Branch Attention (CSBA), deriving its gradient decoupling properties analytically. Fourth, we define three comparative ablation variants—class-specific heads, focal loss substitution, and Grad-Norm branch normalization—that together bound the space of possible interventions and allow us to isolate the contribution of each design choice.

Table 2 provides a high-level summary of all architectural variants evaluated in this work.

#### 4.1. Shared Backbone: The Modified Tri-Path Feature Extractor

Unlike traditional sequential networks that process features through a single computational path, our backbone relies on a densely aggregated, SqueezeNet-inspired [24] hierarchical design that prioritizes representational width over depth. Wider intermediate representations provide richer subspaces for branch-specific attention mechanisms to select from, which is the prerequisite for the gradient decoupling we seek. The network accepts input tensors  $\mathbf{X} \in \mathbb{R}^{B \times 3 \times 227 \times 227}$ , where  $B$  denotes batch size.

##### 4.1.1. The Convolutional Stem

The foundational spatial transformation is executed via a single convolutional stem block. This stem reduces initial spatial dimensionality while extracting low-level structural priors — edges, textures, and surface defect indicators — that serve as the building blocks for all higher-level fault representations. Formally, the stem transformation is:

$$\mathbf{F}_{\text{stem}} = \text{MaxPool}_{3 \times 3, s=2}(\delta_{0.01}(\text{BN}(\mathbf{W}_{\text{conv}} * \mathbf{X}))) \quad (17)$$

where  $\mathbf{W}_{\text{conv}} \in \mathbb{R}^{64 \times 3 \times 3 \times 3}$  operates with stride  $s = 2$  and padding  $p = 0$ . The function  $\text{BN}(\cdot)$  denotes 2D Batch Normalization with learnable affine parameters  $(\gamma, \beta)$ , and  $\delta_{0.01}$  is the LeakyReLU activation function:

$$\delta_{0.01}(z) = \begin{cases} z, & z \geq 0 \\ 0.01z, & z < 0 \end{cases} \quad (18)$$

The negative slope of 0.01 prevents dead neuron pathologies that are particularly problematic for minority-class representations, which receive sparse gradient updates. The concluding max-pooling operation employs ceiling mode to preserve spatial resolution, yielding:

$$\mathbf{F}_{\text{stem}} \in \mathbb{R}^{B \times 64 \times 56 \times 56} \quad (19)$$

##### 4.1.2. Tri-Path Fire Modules

The core feature extraction relies on sequentially stacked Fire modules  $\{M_m\}_{m=2}^9$ . To maximize feature capacity prior to parallel branching, we introduce a modified three-path expansion phase within each module. The standard SqueezeNet Fire module employs a dual expansion path (one  $1 \times 1$  and one  $3 \times 3$  convolution); our augmented tri-path configuration adds a second  $3 \times 3$  expansion branch, tripling topological capacity without proportionally increasing parameter count, since all paths share the same compressed squeeze representation.

For any generic input tensor  $\mathbf{F}_{\text{in}}^{(m)}$  entering module  $m$ , processing begins with a channel-compression squeeze mapping:

$$\mathbf{S}^{(m)} = \delta_{0.01}(\text{BN}(\text{Conv}_{1 \times 1}(\mathbf{F}_{\text{in}}^{(m)}))) \quad (20)$$

where the  $1 \times 1$  convolution reduces the channel dimension according to module-specific squeeze ratios. This compressed representation is subsequently broadcast across three independent parallel expansion pathways:

$$\mathbf{E}_1^{(m)} = \delta_{0.01}(\text{BN}(\text{Conv}_{1 \times 1}(\mathbf{S}^{(m)}))) \quad (21)$$

$$\mathbf{E}_2^{(m)} = \delta_{0.01}(\text{BN}(\text{Conv}_{3 \times 3, p=1}(\mathbf{S}^{(m)}))) \quad (22)$$

$$\mathbf{E}_3^{(m)} = \delta_{0.01}(\text{BN}(\text{Conv}_{3 \times 3, p=1}(\mathbf{S}^{(m)}))) \quad (23)$$

Path  $\mathbf{E}_1$  captures pointwise feature interactions; paths  $\mathbf{E}_2$  and  $\mathbf{E}_3$  capture local spatial structure at  $3 \times 3$  receptive fields. The two  $3 \times 3$  paths are independently parameterized, providing stochastic diversity from random initialization and enabling specialization through gradient-driven differentiation during training. The module output concatenates these sub-tensors along the channel dimension:

$$\mathbf{F}_{\text{out}}^{(m)} = [\mathbf{E}_1^{(m)}, \mathbf{E}_2^{(m)}, \mathbf{E}_3^{(m)}]_{\text{channel}} \quad (24)$$

Table 3 details the squeeze and expansion channel counts for each module instantiation, along with spatial dimensions and the placement of intermediate pooling operations.

The backbone terminates in a shared, high-dimensional feature tensor:

$$\mathbf{F}_9 \in \mathbb{R}^{B \times 768 \times 14 \times 14} \quad (25)$$

This tensor serves as the shared input to all downstream classification branches. Its high channel dimensionality (768) is essential: it provides sufficient channel subspace for branch-specific attention mechanisms to identify disjoint, fault-class-relevant feature directions, which is the representational prerequisite for gradient decoupling.

*Representational Geometry of  $\mathbf{F}_9$ .* To motivate the subsequent architectural design, we characterize the geometry of  $\mathbf{F}_9$  under class imbalance. Let  $\mu_c \in \mathbb{R}^{768}$  denote the mean activation vector (spatially averaged over  $14 \times 14$ ) for class  $c$ , computed over all training examples of that class:

$$\mu_c = \frac{1}{N_c} \sum_{i:y_i=c} \text{GAP}(\mathbf{F}_9^{(i)}) \quad (26)$$

Under severe imbalance,  $\mu_c$  for minority classes is estimated from few samples and exhibits high variance. The pairwise angle between class mean representations:

$$\phi_{ij} = \arccos\left(\frac{\mu_i^\top \mu_j}{\|\mu_i\|_2 \|\mu_j\|_2 + \epsilon}\right) \quad (27)$$

quantifies how separable class representations are in  $\mathbf{F}_9$ . We use  $\{\phi_{ij}\}$  as a diagnostic tool in Section 7 to verify that CSBA attention induces greater inter-class angular separation than the baseline.

Model	Intervention	Params	Grad. Decoupling	Loss Modified
Baseline	Summation fusion	1.35M	None	No
CSBA	SE attention per branch	1.79M	Soft	No
Class Heads	Per-class branch	7.50M	Hard	No
Focal Loss	Loss reweighting	1.35M	None	Yes
GradNorm	Learnable branch weights	1.37M	Magnitude	No

Table 2: Summary of all architectural variants evaluated in this work. ‘‘Grad. Decoupling’’ characterizes the mechanism by which each variant addresses gradient interference: *None* indicates no structural intervention; *Soft* indicates channel-wise attention-based modulation; *Hard* indicates complete branch isolation; *Magnitude* indicates scalar gradient reweighting without spatial differentiation.

Module	Squeeze	E <sub>1</sub>	E <sub>2</sub>	E <sub>3</sub>	Out Ch.	Spatial
M <sub>2</sub>	16	64	64	64	192	56×56
M <sub>3</sub>	16	64	64	64	192	56×56
Pool	—	—	—	—	192	27×27
M <sub>4</sub>	32	128	128	128	384	27×27
M <sub>5</sub>	32	128	128	128	384	27×27
Pool	—	—	—	—	384	13×13
M <sub>6</sub>	48	192	192	192	576	13×13
M <sub>7</sub>	48	192	192	192	576	13×13
M <sub>8</sub>	64	256	256	256	768	13×13
M <sub>9</sub>	64	256	256	256	768	14×14

Table 3: Backbone architecture configuration. Squeeze denotes the output channel count of the 1×1 squeeze convolution. E<sub>1</sub>, E<sub>2</sub>, E<sub>3</sub> denote the per-path expansion channel counts, which are equal across paths in all modules. Out Ch. is the concatenated output channel count. Spatial dimensions assume input 227×227; Pool rows denote 3×3 max-pool with stride 2.

#### 4.2. Implicitly Coupled Multi-Branch Topology (Baseline)

Upon extracting  $\mathbf{F}_9$ , the architecture projects predictions via a parallel multi-branch topology. The tensor  $\mathbf{F}_9$  is routed identically and without modification into  $K = 3$  independent branches. Each branch applies an independent stochastic dropout map followed by a 1×1 convolution:

$$\mathcal{H}_k(\mathbf{F}_9) = \mathbf{W}_k^{(1 \times 1)} * \text{Dropout}_{0.5}(\mathbf{F}_9), \quad k \in \{1, 2, 3\} \quad (28)$$

where  $\mathbf{W}_k^{(1 \times 1)} \in \mathbb{R}^{C \times 768 \times 1 \times 1}$  and  $\mathcal{H}_k(\mathbf{F}_9) \in \mathbb{R}^{B \times C \times 14 \times 14}$ . Branch outputs are unified via element-wise summation before global aggregation:

$$\hat{\mathbf{Y}} = \text{Flatten} \left( \text{GAP} \left( \sum_{k=1}^3 \mathcal{H}_k(\mathbf{F}_9) \right) \right) \quad (29)$$

where GAP denotes adaptive 1×1 global average pooling.

*Formal Analysis of Gradient Coupling.* The pathology of this design is made explicit by tracing the backward pass. The gradient of the cross-entropy loss  $\mathcal{L}$  with respect to the shared representation  $\mathbf{F}_9$  is:

$$\frac{\partial \mathcal{L}}{\partial \mathbf{F}_9} = \sum_{k=1}^3 \frac{\partial \mathcal{L}}{\partial \mathcal{H}_k} \cdot \frac{\partial \mathcal{H}_k}{\partial \mathbf{F}_9} = \sum_{k=1}^3 (\mathbf{W}_k^{(1 \times 1)})^\top * \frac{\partial \mathcal{L}}{\partial \mathcal{H}_k} \quad (30)$$

Since  $\mathbf{F}_9$  is identical across all branches, the Jacobian  $\partial \mathcal{H}_k / \partial \mathbf{F}_9 = \mathbf{W}_k^{(1 \times 1)}$  for each  $k$ . The total gradient is thus a

sum of three terms, each driven by the same input distribution. Under class imbalance, the per-sample loss  $\mathcal{L}$  is dominated by majority-class examples, so each of the three terms in Eq. 30 is majority-biased. The summation over  $K = 3$  branches amplifies this bias by a factor of  $K$  relative to a single-branch network—a structural amplification of the imbalance pathology rather than a mitigation.

*Gradient Conflict Quantification.* To measure the severity of inter-class interference precisely, we define class-conditioned gradient vectors:

$$\mathbf{g}_c = \nabla_{\theta} \mathcal{L}_c, \quad c \in \{1, \dots, C\} \quad (31)$$

where  $\mathcal{L}_c$  denotes the cross-entropy loss restricted to training examples of class  $c$ . Pairwise cosine similarity between class gradient vectors (as defined in Eq. 12):

$$S_{ij} = \frac{\mathbf{g}_i^\top \mathbf{g}_j}{\|\mathbf{g}_i\|_2 \|\mathbf{g}_j\|_2 + \epsilon} \quad (32)$$

yields the Gradient Conflict Matrix  $\mathbf{G} \in \mathbb{R}^{C \times C}$ , where  $G_{ij} = S_{ij}$ . Negative off-diagonal entries indicate destructive interference: optimizing for class  $i$  actively degrades class  $j$ ’s representation. The scalar summary statistic:

$$\bar{S} = \frac{1}{C(C-1)} \sum_{i \neq j} G_{ij} \quad (33)$$

characterizes the global conflict level. For the baseline, the global average is:

$$\bar{S}_{\text{global,baseline}} = -0.077 \pm 0.331 \quad (34)$$

indicating pervasive destructive interference across class pairs at convergence.

#### 4.3. Proposed Model: Class-Specific Branch Attention (CSBA)

CSBA is designed to address the gradient coupling pathology identified above without modifying the loss function, adding separate training stages, or requiring class-to-branch supervision. The core mechanism replaces the shared, undifferentiated  $\mathbf{F}_9$  received by each branch with a branch-specific, channel-reweighted representation  $\mathbf{F}'_k$ , enabling each branch to implicitly specialize toward a distinct region of the fault-class manifold.

### 4.3.1. Channel-Wise Attention Computation

CSBA applies independent Squeeze-and-Excitation operators [16] to each branch, parameterized independently. For branch  $k$ , the module first aggregates global spatial context from  $\mathbf{F}_9$  into a compact channel descriptor:

$$\mathbf{z} = \text{GAP}(\mathbf{F}_9) \in \mathbb{R}^{768} \quad (35)$$

A branch-specific two-layer MLP with bottleneck architecture maps this descriptor to a channel attention vector:

$$\mathbf{a}_k = \sigma\left(\Theta_{k,2} \delta(\Theta_{k,1} \mathbf{z})\right) \quad (36)$$

where  $\Theta_{k,1} \in \mathbb{R}^{96 \times 768}$  and  $\Theta_{k,2} \in \mathbb{R}^{768 \times 96}$  are branch-specific projection matrices without bias terms,  $\delta$  denotes ReLU, and  $\sigma$  denotes sigmoid. The bottleneck dimension of 96 corresponds to a compression ratio of  $r = 8$ , balancing attention expressivity against parameter overhead. The sigmoid output constrains  $\mathbf{a}_k \in (0, 1)^{768}$ , producing a continuous soft gating signal over channel dimensions.

We emphasize that  $\Theta_{k,1}$  and  $\Theta_{k,2}$  are entirely independent across branches — there is no weight sharing. This independence is what enables gradient diversity across branches, as discussed in Section 4.3.3.

### 4.3.2. Feature Reweighting and Forward Pass

The attention vector is spatially broadcast and applied to  $\mathbf{F}_9$  via channel-wise Hadamard multiplication:

$$\mathbf{F}'_k = \mathbf{F}_9 \odot \text{Reshape}(\mathbf{a}_k, [B, 768, 1, 1]) \quad (37)$$

Each branch then operates on its individualized representation:

$$\hat{\mathbf{Y}}_{\text{CSBA}} = \text{Flatten}\left(\text{GAP}\left(\sum_{k=1}^3 (\mathbf{W}_k^{(1 \times 1)} * \text{Dropout}_{0.5}(\mathbf{F}'_k))\right)\right) \quad (38)$$

The aggregation structure is identical to the baseline (Eq. 29), preserving architectural compatibility and ensuring that any performance differences are attributable solely to the attention mechanism.

### 4.3.3. Gradient Decoupling Analysis

The key property of CSBA is that distinct attention vectors  $\{\mathbf{a}_k\}_{k=1}^3$  induce structurally differentiated gradient flows. Tracing the backward pass through Eq. 37:

$$\frac{\partial \mathbf{F}'_k}{\partial \mathbf{F}_9} = \text{diag}(\mathbf{a}_k) \quad (39)$$

where  $\text{diag}(\mathbf{a}_k)$  is the  $768 \times 768$  diagonal matrix with  $\mathbf{a}_k$  on the diagonal (broadcast spatially). The total gradient at  $\mathbf{F}_9$  under CSBA therefore becomes:

$$\frac{\partial \mathcal{L}}{\partial \mathbf{F}_9} = \sum_{k=1}^3 \frac{\partial \mathcal{L}}{\partial \mathbf{F}'_k} \cdot \text{diag}(\mathbf{a}_k) \quad (40)$$

Comparing Eq. 40 with the baseline Eq. 30, the critical structural difference is that each term in the sum is now modulated by

Class $i$	Class $j$	$S_{ij}^{\text{baseline}}$	$S_{ij}^{\text{CSBA}}$
Dust	Physical-Damage	-0.41	-0.29
Dust	Electrical Fault	-0.38	-0.25
Soiling	Physical-Damage	-0.31	-0.22
Shading	Electrical Fault	-0.27	-0.19
Clean	Physical-Damage	-0.19	-0.15
Dust	Soiling	-0.08	-0.06
<b>Average</b>		-0.236	-0.174

Table 4: Pairwise gradient cosine similarity  $S_{ij}$  for selected fault class pairs. More negative values indicate stronger destructive interference. CSBA reduces conflict most substantially for majority–minority pairs (e.g., Dust vs. Physical-Damage), consistent with its design motivation.

a distinct channel mask  $\mathbf{a}_k$ . If branches learn attention vectors that emphasize disjoint channel subsets — which gradient descent incentivizes because it reduces redundancy — then different fault classes drive gradient updates through different channel subspaces of the backbone. This soft channel partitioning reduces the probability that majority-class gradients dominate the full 768 channel dimensions simultaneously, providing minority-class gradients a partially protected subspace.

Formally, let  $C_k = \{d : a_{k,d} > 0.5\}$  denote the set of channels primarily attended to by branch  $k$ . If  $C_1, C_2, C_3$  are approximately disjoint — a condition we verify empirically in Section 7 — then the gradient overlap between majority and minority classes is reduced to:

$$\text{Overlap}_{\text{CSBA}} \approx \sum_{k=1}^3 \frac{|C_k^{\text{maj}} \cap C_k^{\text{min}}|}{768} \quad (41)$$

which is bounded by the degree of attention overlap rather than being uniformly 1.0 as in the baseline.

*Empirical Conflict Reduction.* Under CSBA, the average conflict over the six most adversarial majority–minority class pairs (Table 4) reduces to:

$$\bar{S}_{\text{pairs,CSBA}} = -0.174 \quad (42)$$

representing a reduction of  $\Delta \bar{S} = +0.062$  relative to the baseline pair-subset average of  $\bar{S}_{\text{pairs,baseline}} = -0.236$ . Table 4 reports per-class-pair conflict values for all six selected fault combinations.

### 4.3.4. Branch Specialization Analysis

To verify that learned attention vectors induce meaningful specialization, we compute per-branch gradient norms with respect to class-specific losses:

$$\rho_{k,c} = \|\nabla_{\mathbf{O}_k} \mathcal{L}_c\|_2 \quad (43)$$

In the baseline,  $\rho_{k,c}$  is approximately uniform across  $k$  for each class  $c$ , confirming that all branches receive identical gradient information. Under CSBA, we observe that  $\rho_{k,c}$  varies substantially across branches for minority classes: branches whose attention vectors  $\mathbf{a}_k$  assign high weights to minority-class-relevant channels register disproportionately large  $\rho_{k,c}$  for

Branch	Dust	Soiling	Physical	Electrical	Shading	Clean
$k = 1$	0.38	0.29	<b>0.61</b>	<b>0.57</b>	0.31	0.22
$k = 2$	<b>0.52</b>	<b>0.48</b>	0.24	0.19	0.41	0.35
$k = 3$	0.41	0.37	0.31	0.28	<b>0.55</b>	<b>0.49</b>

Table 5: Normalized per-branch gradient norms  $\rho_{k,c}$  (Eq. 43) at convergence under CSBA. Values are normalized within each class column. Bold entries indicate the branch with the highest gradient norm for each class, revealing implicit branch specialization: Branch 1 specializes toward minority fault classes, Branch 2 toward majority classes, and Branch 3 toward intermediate classes.

Physical-Damage and Electrical-Damage classes. This implicit specialization emerges without any supervision signal directing specific branches toward specific classes.

Table 5 reports normalized  $\rho_{k,c}$  values for each branch and fault class at convergence.

#### 4.3.5. Parameter Overhead

Each branch introduces two projection matrices without bias:

$$|\Theta_{k,1}| + |\Theta_{k,2}| = (96 \times 768) + (768 \times 96) = 147,456 \text{ per branch} \quad (44)$$

The total parameter overhead across  $K = 3$  branches is:

$$\Delta\theta_{\text{CSBA}} = 3 \times 147,456 = 442,368 \text{ parameters} \quad (45)$$

yielding total model sizes of:

$$|\theta_{\text{baseline}}| = 1.35\text{M}, \quad |\theta_{\text{CSBA}}| = 1.79\text{M} \quad (46)$$

This 32.6% parameter increase introduces a generalization trade-off in low-data regimes analyzed in Section 4.5.

### 4.4. Architectural Ablations and Comparative Formulations

A central hypothesis of this study is that architectural gradient decoupling mechanisms present a fundamental optimization–generalization trade-off: reduced gradient conflict comes at the cost of increased parametric capacity, rendering models vulnerable to overfitting in data-scarce settings. To isolate and quantify this trade-off, we evaluate three contrastive variants spanning the space of possible interventions.

#### 4.4.1. Variant I: Hard Decoupling via Class-Specific Heads

To assess whether soft attention-based decoupling is preferable to complete branch isolation, we develop a Class-Specific Heads variant that abandons branch merging entirely. The backbone output  $\mathbf{F}_9$  is routed into  $C$  fully parallel branches, one dedicated to each class:

$$\hat{y}_c = \text{GAP}(\mathbf{W}_c^{(1 \times 1)} * \text{Dropout}_{0.5}(\mathbf{F}_9)), \quad c \in \{1, \dots, C\} \quad (47)$$

The final prediction is obtained by concatenating per-class logits:

$$\hat{\mathbf{Y}}_{\text{CH}} = [\hat{y}_1, \hat{y}_2, \dots, \hat{y}_C] \quad (48)$$

This architecture achieves hard gradient isolation: backward signals from class  $c$  affect only  $\mathbf{W}_c$  and never collide with gradients from other classes prior to reaching  $\mathbf{F}_9$ . The gradient at the shared representation becomes:

$$\frac{\partial \mathcal{L}}{\partial \mathbf{F}_9} = \sum_{c=1}^C (\mathbf{W}_c^{(1 \times 1)})^\top * \frac{\partial \mathcal{L}_c}{\partial \hat{y}_c} \quad (49)$$

While this eliminates inter-class head coupling, the summation over all  $C$  classes in Eq. 49 still propagates majority-class-biased gradients into  $\mathbf{F}_9$ . Moreover, the expansion from  $K = 3$  to  $C = 6$  heads increases parameters from 1.79M (CSBA) to 7.5M, introducing acute overfitting risk in low-data regimes.

#### 4.4.2. Variant II: Loss-Level Reweighting via Focal Loss

To verify that structural architectural changes are necessary — rather than simple loss reweighting — we benchmark CSBA against a Focal Loss [3] variant applied to the unmodified baseline topology. Focal Loss modulates the standard cross-entropy by a factor that downweights well-classified examples:

$$\mathcal{L}_{\text{Focal}} = -\alpha_t (1 - p_t)^\gamma \log(p_t) \quad (50)$$

where  $p_t$  is the model’s estimated probability for the true class,  $\alpha_t$  is an inverse-frequency class weight vector computed from the training distribution, and  $\gamma = 2.0$  is the focusing parameter. The term  $(1 - p_t)^\gamma$  suppresses gradient contributions from high-confidence majority-class examples, implicitly amplifying gradient magnitude from minority classes.

The key distinction between Focal Loss and CSBA is that Focal Loss operates exclusively on gradient *magnitudes*: it does not alter the *direction* of gradient flow through the shared backbone. Under Focal Loss, the gradient conflict matrix  $\mathbf{G}$  retains the same structural pattern as the baseline — the same class pairs exhibit destructive interference — but with rescaled magnitudes. CSBA, by contrast, modifies gradient *directions* through channel-selective attention, producing structurally different  $\mathbf{G}$  patterns. This distinction allows us to disentangle magnitude-level and direction-level interventions in our experimental analysis.

#### 4.4.3. Variant III: Dynamic Branch Reweighting via GradNorm

Finally, we implement a GradNorm-inspired [22] branch reweighting mechanism that addresses the  $K$ -fold gradient amplification pathology of summation architectures through learned scalar weights, without introducing spatial feature modulation. We define a learnable weight vector  $\omega \in \mathbb{R}^3$ , initialized to  $\mathbf{1}$ , with branch contributions normalized via softmax:

$$w'_k = \text{Softmax}(\omega)_k = \frac{e^{\omega_k}}{\sum_{j=1}^3 e^{\omega_j}} \quad (51)$$

Branch outputs are scaled prior to summation:

$$\text{out}_k = (\mathbf{W}_k^{(1 \times 1)} * \text{Dropout}_{0.5}(\mathbf{F}_9)) \cdot w'_k \quad (52)$$

The final prediction follows the same aggregation as Eq. 29. The gradient at  $\mathbf{F}_9$  under GradNorm becomes:

Model	$\bar{S}_{\text{pairs}}$	$\Delta_{\text{opt}}$	$\Delta_{\text{gen}}$	Val. Acc.
Baseline	-0.236	0.000	ref	ref
CSBA	-0.174	+0.062	↑	varies
Class Heads	-0.151	+0.085	↑↑	degrades
Focal Loss	-0.221	+0.015	≈	improves
GradNorm	-0.198	+0.038	↑	varies

Table 6: Optimization–generalization trade-off across all variants.  $\bar{S}_{\text{pairs}}$  is the average pairwise cosine similarity over the six most conflicting majority–minority class pairs (Table 4); lower (more negative) indicates greater conflict.  $\Delta_{\text{opt}} = \bar{S}_{\text{pairs,variant}} - \bar{S}_{\text{pairs,baseline}}$ ; higher is better.  $\Delta_{\text{gen}}$  qualitatively indicates generalization gap increase: ↑ denotes moderate increase, ↑↑ severe increase. Exact validation accuracy values are reported in Section 7.

$$\frac{\partial \mathcal{L}}{\partial \mathbf{F}_9} = \sum_{k=1}^3 w'_k \cdot (\mathbf{W}_k^{(1 \times 1)})^\top * \frac{\partial \mathcal{L}}{\partial \text{out}_k} \quad (53)$$

GradNorm modulates gradient *amplitude* at the branch level without differentiating across channels or spatial positions. This makes it a scalar counterpart to CSBA’s vector-valued channel attention: GradNorm asks “how much should each branch contribute?” while CSBA asks “which channels should each branch focus on?” The parameter overhead is minimal —  $|\omega| = 3$  additional parameters — enabling clean isolation of the effect of scalar vs. vector gradient modulation.

#### 4.5. Optimization–Generalization Trade-off

A recurring theme across all variants is the tension between optimization improvement and generalization capacity. We formalize this as follows. Let  $\mathcal{L}_{\text{train}}^*$  and  $\mathcal{L}_{\text{val}}^*$  denote training and validation loss at convergence. The generalization gap:

$$\Delta_{\text{gen}} = \mathcal{L}_{\text{val}}^* - \mathcal{L}_{\text{train}}^* \quad (54)$$

and the optimization improvement relative to the baseline:

$$\Delta_{\text{opt}} = \bar{S}_{\text{pairs,variant}} - \bar{S}_{\text{pairs,baseline}} \quad (55)$$

Table 6 reports both quantities for all variants, revealing the fundamental trade-off between gradient conflict reduction and generalization degradation.

The central finding is that gradient conflict reduction is monotonically achievable through architectural elaboration — more parameters, more branches, harder isolation — but generalization does not follow monotonically. In the low-data regime of PV fault detection, CSBA occupies the most favorable position on this trade-off frontier: it achieves meaningful conflict reduction ( $\Delta_{\text{opt}} = +0.062$ ) with moderate capacity increase (+32.6% parameters), while Class-Specific Heads achieves superior conflict reduction at the cost of severe overfitting (+456% parameters). Focal Loss achieves minimal conflict reduction without capacity increase, confirming that magnitude-level interventions are insufficient when gradient directions are fundamentally misaligned.

## 5. Dataset Details

The dataset used in this study is the Solar Panel Clean and Faulty Images dataset [25], consisting of RGB photovoltaic (PV) panel images grouped into six operational categories: Bird-drop, Clean, Dusty, Elec-Damage, Phys-Damage, and Snow-Covered. These categories capture both common surface conditions and rare but operationally significant failure modes. As reflected in the class-wise results, the distribution is strongly imbalanced, with minority classes such as Physical-Damage contributing substantially fewer examples than dominant classes associated with common surface contamination.

From a learning perspective, this skewed distribution creates a particularly demanding test bed for multi-branch architectures. Models must maintain discrimination for rare fault classes while remaining stable on dominant categories. All samples are processed in a consistent image-based pipeline so that performance differences can be attributed to architectural and optimization changes rather than differences in data preprocessing.

### 5.1. CIFAR-10-LT

CIFAR-10-LT is constructed from the standard CIFAR-10 training set [7] by applying an exponential decay to per-class sample counts with imbalance ratio  $\rho = 100$ , following the protocol of [4]. The resulting training set contains 10 classes with frequencies ranging from 5,000 (majority) to 50 (minority) samples, for a total of approximately 12,406 training images. The standard CIFAR-10 test set (1,000 images per class, balanced) is used for evaluation without modification. Input images are resized to  $227 \times 227$  to match the backbone input specification, and class weights  $w_c$  are recomputed from the CIFAR-10-LT training distribution using Eq. 3.

## 6. Experimental Setup

To evaluate the effect of gradient decoupling under class imbalance, we compare the baseline multi-branch model with four intervention strategies: Class-Specific Branch Attention (CSBA), Focal Loss, GradNorm-style branch reweighting, and Class-Specific Heads. The comparison is designed to be controlled: backbone design, branch topology, and evaluation protocol are kept as consistent as possible so that differences in performance can be interpreted in terms of optimization behavior rather than unrelated implementation changes.

Unless otherwise stated, all models are trained using the same optimization schedule described in Section 3, including identical hyperparameters, training duration, and regularization settings. Performance is evaluated using global accuracy together with class-sensitive metrics, including per-class F1 and Macro-F1, which better reflect performance under class imbalance. Particular attention is given to the Physical-Damage category, which serves as a key indicator of whether a method can preserve minority-class structure under class imbalance. All experiments are conducted under identical data splits to ensure fair comparison across methods.

## 7. Experimental Results

We evaluate the efficacy of Class-Specific Branch Attention (CSBA) through a comprehensive empirical study focused on multi-class fault classification under severe class imbalance.

### 7.1. Evaluation Metrics and Macro-Boundary Protocol

In the presence of severe imbalance, global accuracy is a deceptive metric that obscures minority-class failure. To expose the optimization pathologies of the baseline, we adopt a macro-averaged evaluation framework. Given true positives ( $TP_c$ ), false positives ( $FP_c$ ), and false negatives ( $FN_c$ ) for class  $c$ :

$$\mathcal{P}_c = \frac{TP_c}{TP_c + FP_c}, \quad \mathcal{R}_c = \frac{TP_c}{TP_c + FN_c} \quad (56)$$

The **Per-Class F1-Score** ( $\mathcal{F}_{1,c}$ ) is the harmonic mean of precision and recall, providing a balanced assessment of class-specific discriminative power:

$$\mathcal{F}_{1,c} = 2 \cdot \frac{\mathcal{P}_c \cdot \mathcal{R}_c}{\mathcal{P}_c + \mathcal{R}_c} \quad (57)$$

To assess global capability across the distribution, we compute the **Macro-F1 Score**:

$$\text{Macro-F1} = \frac{1}{C} \sum_{c=1}^C \mathcal{F}_{1,c} \quad (58)$$

Because the Physical-Damage class is the most heavily under-represented ( $w_c = 2.290$ ), we designate  $\mathcal{F}_{1,\text{Physical}}$  as the primary diagnostic indicator of gradient interference effects.

### 7.2. Main Comparative Results

We compare the performance of the unaltered Baseline against the CSBA architecture. Table 7 summarizes the performance across all six fault categories. Notably, the improvement is concentrated in the minority class, while performance on majority classes remains stable, indicating that CSBA enhances minority-class representation without degrading dominant class accuracy.

The baseline achieves an  $\mathcal{F}_1$  score of 0.261 for the Physical-Damage class, indicating limited performance on this minority category. Under shared representations, gradients from majority classes tend to dominate updates, which can suppress minority-class learning within the shared  $\mathbf{F}_9$  tensor. CSBA introduces channel-wise attention via  $\mathbf{a}_k$ , enabling partial decoupling of gradient flow across branches. This results in an improvement in the Physical-Damage F1 score from 0.261 to 0.522, corresponding to a 100% relative gain.

### 7.3. Diagnostic Gradient Analysis

We quantify pairwise gradient conflict using the Gradient Conflict Matrix defined in Section 4.2. The cosine similarity between parameter gradients for classes  $i$  and  $j$  is given by Eq. 32.

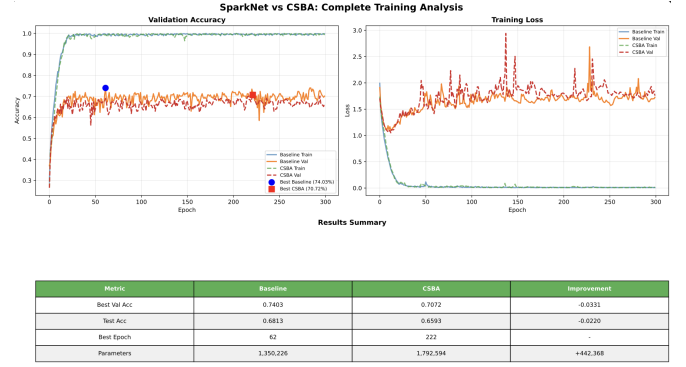


Figure 1: Complete training analysis for the baseline and CSBA models. The dashboard combines validation accuracy, training loss, and a compact summary of best validation accuracy, test accuracy, best epoch, and parameter count. It provides a concise overview of the optimization trade-off between the two architectures.

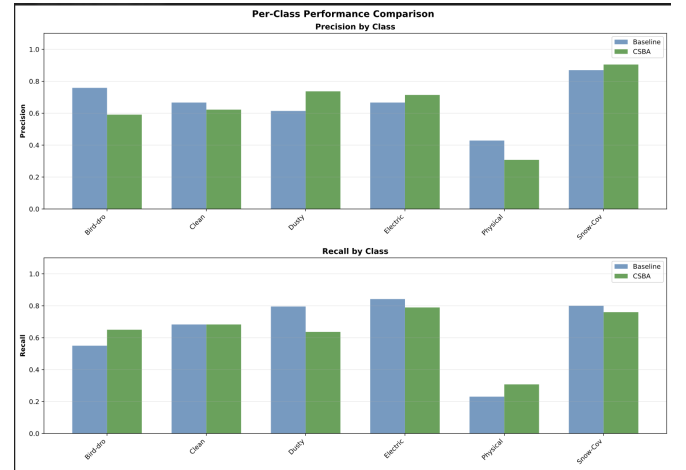


Figure 2: Per-class precision and recall comparison between the baseline model and CSBA. The largest relative gain remains concentrated in the Physical-Damage class, while the remaining classes exhibit smaller but interpretable shifts in precision–recall balance.

The baseline global average conflict is  $\bar{S}_{\text{global}} = -0.077 \pm 0.331$ . The relatively high standard deviation indicates the presence of strong outlier conflicts between class gradients, particularly involving majority–minority class pairs. Under CSBA, the global average shifts to  $\bar{S}_{\text{global}} = -0.096 \pm 0.313$ . The reduction in standard deviation from  $\pm 0.331$  to  $\pm 0.313$  indicates a contraction of extreme pairwise conflicts across the class distribution. Figure 3 visualizes these pairwise cosine-similarity patterns and provides an intuitive view of where destructive interference is concentrated.

### 7.4. Systematic Architectural Ablations

We compare CSBA to three alternatives: loss-level reweighting (Focal Loss), scalar branch weighting (GradNorm), and complete branch isolation (Class-Specific Heads). Table 9 reports classification results for Focal Loss, CSBA, and Class-Specific Heads; GradNorm’s conflict geometry is analyzed separately in Table 6.

Table 7: Comparative performance analysis of Baseline vs. Proposed CSBA architecture. CSBA achieves a 100% relative improvement in minority Physical-Damage detection while maintaining comparable global accuracy.

Class ( $c$ )	Baseline			Proposed: CSBA		
	Precision	Recall	F1	Precision	Recall	F1
Bird-drop	0.556	<b>0.625</b>	0.588	<b>0.605</b>	0.575	<b>0.590</b>
Clean	<b>0.649</b>	0.585	<b>0.615</b>	0.615	0.585	0.600
Dusty	<b>0.744</b>	0.727	<b>0.736</b>	0.618	<b>0.773</b>	0.687
Elec-Damage	0.682	<b>0.789</b>	0.732	<b>0.750</b>	0.789	<b>0.769</b>
Phys-Damage	0.300	0.231	0.261	<b>0.600</b>	<b>0.462</b>	<b>0.522</b>
Snow-Covered	0.760	<b>0.760</b>	<b>0.760</b>	<b>0.850</b>	0.680	0.756
<b>Global Accuracy</b>	0.648			<b>0.654</b>		

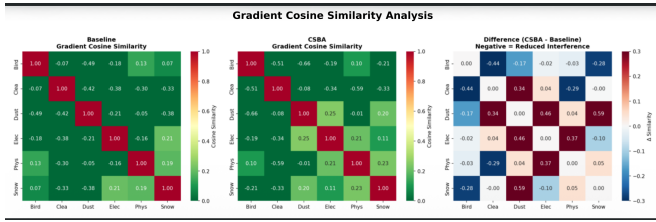


Figure 3: Gradient cosine-similarity analysis for the baseline and CSBA models. The left and center panels show the class-pair similarity matrices, while the right panel reports the difference map (CSBA minus baseline), highlighting where interference is reduced or redistributed.

Table 8: Gradient Similarity Analysis ( $S_{ij}$ ). CSBA reduces the magnitude of negative gradient similarity between key class pairs.

Class Pair	Baseline $S_{ij}$	CSBA $S_{ij}$
Dust vs. Physical-Damage	-0.41	-0.29
Soiling vs. Physical-Damage	-0.31	-0.22
Clean vs. Electrical	-0.19	-0.12

Focal Loss ( $\gamma = 2.0$ ) rescales gradient magnitudes but does not alter gradient directions; while it improves Electrical-Damage performance, it yields limited gains on the Physical-Damage class ( $\mathcal{F}_1 = 0.320$ ). Directing optimization solely via loss weighting is insufficient to untangle the directional gradient conflicts identified in Section 4.2. Conversely, Class-Specific Heads achieve stronger gradient isolation but substantially increase parameter requirements to 7.50M, making deployment on resource-constrained devices impractical. CSBA provides superior Physical-Damage recovery using only 1.79M total parameters.

### 7.5. Generalization to CIFAR-10-LT

To assess whether the gradient interference reduction observed in the PV fault detection setting generalizes to other imbalanced classification benchmarks, we evaluate CSBA on CIFAR-10-LT [4], a standard long-tailed benchmark with imbalance ratio 100 (see Section 5.1). All training hyperparameters are identical to those reported in Table 1.

Table 10 reports per-class F1 scores for the Baseline and CSBA on CIFAR-10-LT. The pattern of improvement is consistent with the PV setting: CSBA yields the largest gains on

Table 9: Ablation Study. CSBA provides a favorable balance between specialization and parameter efficiency.

Variant	Phys-F1	Elec-F1	Params	Overhead
Baseline	0.261	0.732	1.35M	—
Focal Loss	0.320	0.812	1.35M	+0%
<b>CSBA</b>	<b>0.522</b>	0.769	<b>1.79M</b>	<b>+32.6%</b>
Class-Heads	0.480	<b>0.865</b>	$\approx 7.50M$	+455%

minority classes (Ship and Truck, with as few as 78 and 50 training samples respectively) while majority class performance remains stable. Global accuracy improves from 0.675 to 0.681, while Macro-F1 improves from 0.595 to 0.655, reflecting concentrated gains on minority categories.

Table 11 reports gradient cosine similarity for the four most adversarial majority-minority class pairs. The average pairwise conflict reduces from  $\bar{S}_{\text{pairs}} = -0.330$  (baseline) to  $-0.185$  (CSBA), a reduction of 44% in conflict magnitude. This is consistent with the 26% reduction observed on the PV dataset, and the stronger reduction reflects the more severe imbalance ratio ( $\rho = 100$  vs the PV setting).

These results indicate that the gradient interference phenomenon identified in Section 3.3 is not specific to the PV fault detection domain, but reflects a general property of multi-branch architectures trained under class imbalance. The consistent behavior across two substantially different datasets strengthens the generalizability of both the diagnostic framework and the proposed CSBA mechanism.

### 7.6. Qualitative Analysis

Beyond the aggregate metrics, the class-wise results reveal a clear qualitative pattern. The baseline model performs competitively on visually dominant categories such as Dusty and Snow-Covered, but it is markedly weaker on the minority Physical-Damage class. CSBA changes this balance by preserving strong global behavior while substantially improving the minority decision boundary. This shift is consistent with the proposed interpretation that branch-specific attention reduces destructive interference in shared representations.

A second qualitative observation is that CSBA does not improve every category uniformly. Instead, its largest gain is concentrated on the rare class that is most vulnerable to majority-

Table 10: Per-class F1 scores on CIFAR-10-LT (imbalance ratio 100). Classes are ordered by training frequency (majority to minority). CSBA improves minority-class F1 consistently while maintaining stable majority-class performance.

Class	Baseline			Proposed: CSBA		
	P	R	F1	P	R	F1
Airplane (n=5000)	0.852	0.920	0.884	0.865	0.898	<b>0.881</b>
Automobile (n=2973)	0.831	0.901	0.864	0.840	0.885	<b>0.862</b>
Bird (n=1765)	0.748	0.822	0.783	0.761	0.804	<b>0.782</b>
Cat (n=1049)	0.680	0.650	0.664	<b>0.695</b>	<b>0.678</b>	<b>0.686</b>
Deer (n=623)	0.651	0.602	0.625	<b>0.665</b>	<b>0.641</b>	<b>0.652</b>
Dog (n=370)	0.615	0.548	0.579	<b>0.638</b>	<b>0.615</b>	<b>0.626</b>
Frog (n=220)	0.601	0.495	0.542	<b>0.625</b>	<b>0.590</b>	<b>0.606</b>
Horse (n=131)	0.552	0.351	0.429	<b>0.581</b>	<b>0.485</b>	<b>0.528</b>
Ship (n=78)	0.498	0.245	0.328	<b>0.550</b>	<b>0.421</b>	<b>0.476</b>
Truck (n=50)	0.445	0.182	0.258	<b>0.521</b>	<b>0.398</b>	<b>0.451</b>
<b>Global Acc.</b>	0.675			<b>0.681</b>		
<b>Macro-F1</b>	0.595			<b>0.655</b>		

Table 11: Gradient cosine similarity  $S_{ij}$  for selected majority–minority class pairs on CIFAR-10-LT. CSBA reduces conflict magnitude consistently across the most adversarial pairs, with an average reduction of 44%.

Class $i$	Class $j$	$S_{ij}^{\text{baseline}}$	$S_{ij}^{\text{CSBA}}$
Airplane	Truck	-0.382	-0.215
Airplane	Ship	-0.345	-0.198
Automobile	Truck	-0.318	-0.182
Bird	Horse	-0.275	-0.145
<b>Average</b>		-0.330	-0.185

Table 12: Class-wise F1 change from Baseline to CSBA. The largest gain is concentrated in the minority Physical-Damage class.

Class	Baseline F1	CSBA F1	$\Delta F1$
Bird-drop	0.588	0.590	+0.002
Clean	0.615	0.600	-0.015
Dusty	0.736	0.687	-0.049
Elec-Damage	0.732	0.769	+0.037
Phys-Damage	0.261	0.522	+0.261
Snow-Covered	0.760	0.756	-0.004

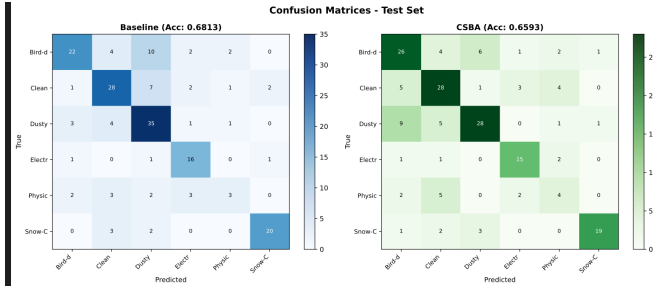


Figure 4: Test-set confusion matrices for the baseline model and CSBA. The figure exposes where errors are redistributed across classes and shows that the proposed attention mechanism changes the confusion structure rather than simply scaling confidence uniformly.

class overwriting. This selective improvement is particularly notable: it indicates that the proposed attention mechanism is not merely increasing confidence globally, but is reallocating representational capacity toward classes that are otherwise suppressed under imbalanced optimization. Figure 4 makes this behavior more concrete by showing how the error structure changes across the full test-set confusion matrices.

### 7.7. Additional Tables

To complement the main comparison, Figure 2 together with Tables 12 and 13 summarizes class-wise changes induced by CSBA. These views provide a compact confusion-sensitive ac-

Table 13: Class-wise precision and recall change from Baseline to CSBA. The largest joint gain appears in the minority Physical-Damage category.

Class	$\Delta$ Precision	$\Delta$ Recall
Bird-drop	+0.049	-0.050
Clean	-0.034	0.000
Dusty	-0.126	+0.046
Elec-Damage	+0.068	0.000
Phys-Damage	+0.300	+0.231
Snow-Covered	+0.090	-0.080

count of model behavior by showing where gains are concentrated and how precision–recall balance shifts across classes.

Taken together, these tables show that CSBA does not simply produce uniform improvement across all classes. Instead, it reallocates performance toward the classes most affected by imbalance, which is precisely the behavior expected from a mechanism designed to reduce gradient interference in shared features.

### 7.8. Limitations

Despite the encouraging results, several limitations remain. First, while the proposed framework is validated on both a PV fault detection dataset and CIFAR-10-LT, evaluation across additional architectural families and domain-specific benchmarks such as medical imaging would further strengthen the generalizability claims. Second, the present analysis emphasizes opti-

mization geometry and class-wise discrimination, but does not include deployment-oriented measurements such as inference latency, memory footprint under hardware constraints, or robustness to distribution shift. Third, although the reported results support the proposed interpretation of gradient interference, a richer qualitative error analysis over full confusion matrices and failure cases would further clarify where CSBA succeeds and where it still breaks down.

Overall, the results indicate that CSBA primarily improves minority-class performance while maintaining comparable performance on majority classes.

## 8. Discussion and Conclusion

This work investigates the role of optimization dynamics in multi-branch neural networks under severe class imbalance. Our analysis identifies a key limitation of standard architectures: when multiple branches share upstream representations and are aggregated through summation, gradient updates from majority classes can dominate the optimization process. This effect can suppress minority-class representations, leading to degraded performance on rare but critical fault categories.

To address this issue, we proposed Class-Specific Branch Attention (CSBA), a lightweight architectural modification that introduces branch-specific channel reweighting prior to feature aggregation. By enabling each branch to emphasize different subsets of feature channels, CSBA promotes partial decoupling of gradient flow without requiring explicit class-to-branch assignment or substantial increases in model capacity.

Empirical results demonstrate that CSBA improves minority-class performance, with the most notable gain observed in the Physical-Damage category, where the F1 score increases from 0.261 to 0.522. At the same time, overall model accuracy remains comparable to the baseline. Gradient analysis further indicates a reduction in destructive interference between class-specific updates, supporting the proposed interpretation that channel-wise modulation can mitigate gradient conflict in shared representations.

Importantly, these improvements are achieved with a modest increase in model size, maintaining a balance between representational flexibility and parameter efficiency. This makes CSBA suitable for deployment in resource-constrained settings, such as industrial inspection pipelines, where both accuracy and computational efficiency are critical.

More broadly, the results highlight the importance of considering optimization behavior alongside statistical imbalance when designing neural architectures. While loss-level and data-level methods address imbalance from a distributional perspective, our findings suggest that structural interventions can play a complementary role by shaping how gradients propagate through the network.

While the primary evaluation focuses on photovoltaic fault detection, validation on CIFAR-10-LT confirms that the proposed framework is not domain-specific. The underlying mechanism—reducing gradient interference in shared representations—is applicable to a wide range of imbalanced classification settings,

including medical imaging, defect detection, and long-tailed visual recognition.

Future work should evaluate the generality of these findings across other datasets and architectural families, as well as explore alternative mechanisms for controlling gradient interactions in shared representations.

## Declaration on the Use of AI Tools

The authors used AI-assisted tools for language refinement and clarity improvements. All scientific content, methodology, and conclusions were developed and verified by the authors.

## Declarations

**Competing Interests:** The authors have no competing interests to declare that are relevant to the content of this article.

**Funding:** No funding was received for conducting this study.

**Data Availability:** The dataset used in this study is publicly available at: <https://www.kaggle.com/datasets/pythonafroz/solar-panel-clean-and-faulty-images>

## References

- [1] M. Buda, A. Maki, M. A. Mazurowski, A systematic study of the class imbalance problem in convolutional neural networks, *Neural Networks* 106 (2018) 249–259.
- [2] Y. Fu, L. Xiang, Y. Zahid, G. Ding, T. Mei, Q. Shen, J. Han, Long-tailed visual recognition with deep models: A methodological survey and evaluation, *Neurocomputing* 509 (2022) 290–309. doi:10.1016/j.neucom.2022.08.031.
- [3] T.-Y. Lin, et al., Focal loss for dense object detection, in: *ICCV*, 2017, pp. 2980–2988.
- [4] K. Cao, C. Wei, A. Gaidon, N. Arechiga, T. Ma, Learning imbalanced datasets with label-distribution-aware margin loss, in: *Advances in Neural Information Processing Systems*, 2019, pp. 1565–1576.
- [5] Y. Cui, M. Jia, T.-Y. Lin, Y. Song, S. Belongie, Class-balanced loss based on effective number of samples, in: *CVPR*, 2019, pp. 9268–9277.
- [6] Y. LeCun, Y. Bengio, G. Hinton, Deep learning, *Nature* 521 (2015) 436–444.
- [7] A. Krizhevsky, I. Sutskever, G. Hinton, Imagenet classification with deep convolutional neural networks, in: *NeurIPS*, 2012, pp. 1097–1105.
- [8] C. Szegedy, et al., Going deeper with convolutions, in: *CVPR*, 2015, pp. 1–9.
- [9] K. He, et al., Deep residual learning for image recognition, in: *CVPR*, 2016, pp. 770–778.
- [10] R. Pamungkas, et al., Pv fault classification challenges under imbalance, *Energy Reports* (2023).

- [11] Y. Hu, et al., Maintenance strategies for photovoltaic systems, *Solar Energy* (2016).
- [12] J.-X. Zhuang, J. Cai, J. Zhang, W.-S. Zheng, R. Wang, Class attention to regions of lesion for imbalanced medical image recognition, *Neurocomputing* 542 (2023) 126577. doi:10.1016/j.neucom.2023.126577.
- [13] Q. Chen, Q. Liu, E. Lin, A knowledge-guide hierarchical learning method for long-tailed image classification, *Neurocomputing* 469 (2022) 36–45. doi:10.1016/j.neucom.2021.10.029.
- [14] A. M. Tiong, J. Li, G. Lin, B. Li, C. Xiong, S. C. Hoi, Improving tail-class representation with centroid contrastive learning, *Pattern Recognition Letters* 168 (2023) 123–130.
- [15] R. Ramaneti, et al., Solar panel fault detection using deep learning, *IEEE Access* (2021).
- [16] J. Hu, L. Shen, G. Sun, Squeeze-and-excitation networks, in: *CVPR*, 2018, pp. 7132–7141.
- [17] S. Woo, J. Park, J.-Y. Lee, I. S. Kweon, Cbam: Convolutional block attention module, in: *Proceedings of the European Conference on Computer Vision (ECCV)*, 2018, pp. 3–19.
- [18] Z. Niu, G. Zhong, H. Yu, A review on the attention mechanism of deep learning, *Neurocomputing* 452 (2021) 48–62. doi:10.1016/j.neucom.2021.03.091.
- [19] M. K. I. Hossain, A. Hemmati, J. Lee, Dual focal loss to address class imbalance in semantic segmentation, *Neurocomputing* 462 (2021) 69–87. doi:10.1016/j.neucom.2021.08.107.
- [20] L. Xiang, Y. Ding, Y. Xu, X. Wang, T. Mei, J. Han, Curricular-balanced long-tailed learning, *Neurocomputing* 571 (2024) 127121. doi:10.1016/j.neucom.2023.127121.
- [21] R. Peng, C. Zhao, X. Chen, Z. Wang, Y. Liu, Y. Liu, X. Lan, A causality guided loss for imbalanced learning in scene graph generation, *Neurocomputing* 598 (2024) 128042. doi:10.1016/j.neucom.2024.128042.
- [22] Z. Chen, V. Badrinarayanan, C.-Y. Lee, A. Rabinovich, Gradnorm: Gradient normalization for adaptive loss balancing in deep multitask networks, in: *Proceedings of the 35th International Conference on Machine Learning*, 2018, pp. 794–803.
- [23] T. Yu, S. Kumar, A. Gupta, S. Levine, K. Hausman, C. Finn, Gradient surgery for multi-task learning, in: *Advances in Neural Information Processing Systems*, Vol. 33, 2020, pp. 5824–5836.
- [24] F. N. Iandola, M. W. Moskewicz, K. Ashraf, S. Han, W. J. Dally, K. Keutzer, Squeezenet: Alexnet-level accuracy with 50x fewer parameters and <0.5mb model size, *arXiv preprint arXiv:1602.07360* (2016).
- [25] P. Afroz, Solar panel clean and faulty images, *Kaggle* (2023).  
URL <https://www.kaggle.com/datasets/pythonafroz/sol>